Nanoscale Advances

ROYAL SOCIETY OF CHEMISTRY

COMMUNICATION

View Article Online
View Journal | View Issue

Cite this: *Nanoscale Adv.*, 2020, **2**, 2752

Received 12th February 2020
Accepted 15th June 2020

DOI: 10.1039/d0na00117a

rsc.li/nanoscale-advances

Mn(II) chelate-coated superparamagnetic iron oxide nanocrystals as high-efficiency magnetic resonance imaging contrast agents†

Changqiang Wu, ‡[a] Tianwu Chen,‡[a] Lihua Deng,[ac] Qian Xia,[a] Chuan Chen,[b] Mu Lan,[a] Yu Pu,[a] Hongjie Tang,[d] Ye Xu,[e] Jiang Zhu,*[ab] Chenjie Xu,[f] Chengyi Shen[a] and Xiaoming Zhang*[a]

In this communication, a paramagnetic bifunctional manganese(II) chelate ([Mn(Dopa-EDTA)]$^{2-}$) containing a catechol group is designed and synthesized. The catechol can bind iron ions on the surface of superparamagnetic iron oxide (SPIO) nanocrystals to form core–shell nanoparticles. Both 4 and 7 nm SPIO@[Mn(Dopa-EDTA)]$^{2-}$ show good water solubility, single-crystal dispersion, and low cytotoxicity. The study of the interplay between the longitudinal and transverse relaxation revealed that 4 nm SPIO@[Mn(Dopa-EDTA)]$^{2-}$ with lower $r_2/r_1 =$ 1.75 at 0.5 T tends to be a perfect T_1 contrast agent while 7 nm SPIO@[Mn(Dopa-EDTA)]$^{2-}$ with a higher $r_2/r_1 = 15.0$ at 3.0 T tends to be a T_2 contrast agent. Interestingly, 4 nm SPIO@[Mn(Dopa-EDTA)]$^{2-}$ with an intermediate value of $r_2/r_1 = 5.26$ at 3.0 T could act as T_1–T_2 dual-modal contrast agent. *In vivo* imaging with the 4 nm SPIO@[Mn(Dopa-EDTA)]$^{2-}$ nanoparticle shows unique imaging features: (1) long-acting vascular imaging and different signal intensity changes between the liver parenchyma and blood vessels with the CEMRA sequence; (2) the synergistic contrast enhancement of hepatic imaging with the T_1WI and T_2WI sequence. In summary, these Fe/Mn hybrid core–shell nanoparticles, with their ease of synthesis, good biocompatibility, and synergistic contrast enhancement ability, may provide a useful method for tissue and vascular MR imaging.

Magnetic resonance imaging (MRI) is one of the most powerful non-invasive medical diagnostic imaging modalities which can offer high spatial resolution and tissue contrast imaging, without ionizing radiation.[1] The nuclear magnetic resonance (NMR) signal of clinical MRI mainly comes from protons of water, which is about 65% of human body weight. The desired MR image contrast between different biological tissues could be created from the weighting image of their intrinsic physical parameters: longitudinal time (T_1), transversal time (T_2), T_2^* and proton density (ρ).[2]

Despite the inherent contrast being obtained, there remains a need for contrast agents (CAs) in MRI to further delineate the structure, enhance tissue differentiation and monitor physiological functions. Now, more than one third (1/3) routine clinical MR scans are contrast-enhanced with the paramagnetic chelates of gadolinium-based contrast agents (GBCAs).[3,4] MRI CAs can catalytically shorten the relaxation times of bulk water protons and their efficiency is measured by relaxivity (r_i, $i = 1$, 2), which is defined as the change in the relaxation rate ($\Delta(R_{1,2}) = \Delta(1/T_{1,2})$, in units of s^{-1}) of the water protons upon addition of 1 mM CAs.[5]

MR CAs can be categorized as either T_1 or T_2 CAs based on their effects being more pronounced for either T_1 or T_2. T_1 CAs (positive contrast agents), such as the paramagnetic chelates of gadolinium (Gd^{3+}), iron (Fe^{3+}) or manganese (Mn^{2+}) ions with low r_2/r_1 (approximately 1), can increase the signal intensity and produce bright images in a T_1-weighted sequence.[6] Typical T_1 CAs such as the FDA approved nine GBCAs are small molecules with poor relaxation efficiency and short circulation time in the vascular system because of their fast tumbling in solution and rapid renal excretion.[7]

On the other hand, T_2 CAs (negative contrast agents), such as magnetic nanoparticles with a very high r_2 value (up to 500 $mmol^{-1}$ s^{-1}) and high r_2/r_1 ratio, can significantly decrease the signal intensity and produce dark images in a T_2 or T_2^*-weighted sequence.[8] However, because the "black holes" effect produced by the large magnetic susceptibility of nanoparticles, the T_2 dark images of nanoparticle labelled lesions sometimes will confused with low signal noise ratio (SNR) areas such as calcification, air, hemorrhage, and blood clots.[9,10]

[a]Sichuan Key Laboratory of Medical Imaging and School of Medical Imaging, Affiliated Hospital of North Sichuan Medical College, Nanchong 637000, China. E-mail: zhujiang@nsmc.edu.cn; zhangxm@nsmc.edu.cn

[b]School of Pharmacy, North Sichuan Medical College, Nanchong 637000, China

[c]Department of Radiology, First People's Hospital of Neijiang, Neijiang 641000, China

[d]Department of Radiology, Nanchong Hospital of Traditional Chinese Medicine, Nanchong 637000, China

[e]Department of Radiology, Children's Hospital of Chongqing Medical University, Chongqing 401122, China

[f]School of Chemical and Biomedical Engineering, Nanyang Technological University, Singapore

† Electronic supplementary information (ESI) available. See DOI: 10.1039/d0na00117a

‡ C. W. and T. C. contributed equally to this work.

T_1 and T_2 weighted imaging, with an accurate match of spatial and temporal imaging parameters can provide the cross-validation information in MRI, are routinely proceeded usually in clinical diagnostic work.[11,12] Moreover, T_1–T_2 dual-modal CAs are necessary, which can produce effective contrast enhancement in both T_1 and T_2 weighted imaging.[13] The ideal T_1–T_2 dual-modal CAs should have high T_1 and T_2 relaxivities (r_1 and r_2) and intermediate r_2/r_1 ratios (about 5–8).[14] Recently, several attempts have been made to design T_1–T_2 dual-modal CAs based on magnetic nanoparticles, and its r_1, r_2 and r_2/r_1 ratio can be tuned by modulating their crystal size, composition, and surface state.[15–17] For example, ultra-small superparamagnetic iron oxide (SPIO),[18–21] paramagnetic metal (such as Gd and Mn) doping[22–25] or paramagnetic metal oxide (such as MnO and Gd_2O_3) coating core/shell[26–30] SPIO nanocrystals with a desired r_2/r_1 ratio have been reported. On the other hand, optimizing the rotational correlation time (τ_R) of small molecular gadolinium complexes by conjugating them onto the surface of SPIO nanoparticles is another effective approach to build T_1–T_2 dual-modal CAs.[31–34]

The design of CAs with clinical application prospects should take into account efficacy and biosafety simultaneously. Over the last decade, there is increasing concern about the safety of using GBCAs due to nephrogenic systemic fibrosis (NSF) and gadolinium retention,[35–39] and much emphasis is now being put on alternative approaches based on non-lanthanide metals, in particular, more biocompatible manganese by scientists.[40–44] However, the direct use of free Mn or manganese oxide also has neurotoxicity risks, and a stable Mn(II) chelate and low Mn dosages are needed. In our previous work, Mn based CAs with good stability and efficacy were developed by optimizing the ligand structure.[7,45–50] In this paper, we seek to design a new bifunctional Mn(II) chelate containing a catechol group, which possesses a high affinity for iron(III)[31,51–54], to coat on the surface of SPIO nanocrystals for forming non-gadolinium-based nanoscale CAs (Fig. 1a). To explore the performance in MRI, we studied its morphology, composition, aggregate states, relaxation properties and imaging effect *in vivo*.

The bifunctional ligand (named Dopa-EDTA) with a catechol group and EDTA structure was synthesized from Dopa, and the detailed synthesis steps and the characterization data of intermediates can be found in the ESI.† The chelate of $[Mn(Dopa\text{-}EDTA)]^{2-}$ was confirmed from the ESI Mass spectrum (Fig. 1b). Monodispersed SPIO nanocrystals were synthesized by thermal decomposition of iron acetylacetonate.[55] Two hydrophobic SPIO nanoparticles with different crystal size distributions were obtained respectively in different reaction solvents and the corresponding water soluble SPIO@$[Mn(Dopa\text{-}EDTA)]^{2-}$ nanoparticles can be easily obtained by ligand exchange with $[Mn(Dopa\text{-}EDTA)]^{2-}$ (the synthetic procedure can be found in the ESI†). To study the crystal type, size and dispersity of nanoparticles, transmission electron microscopy (TEM) and the dynamic light scattering (DLS) technique were used before and after ligand exchange. As shown in Fig. 1c, both SPIO nanoparticles showed good monodispersion in TEM, and the lattice fringes are clearly visible in the high-resolution TEM (HRTEM) images. These results indicated that the particles are single crystals with monodispersion being maintained before and after ligand exchange. Crystal sizes were measured from select different representative areas under a TEM and were 3.7 ± 0.7 nm and 6.6 ± 1.0 nm respectively for the two sizes of SPIO nanoparticles. In the following text, the corresponding samples

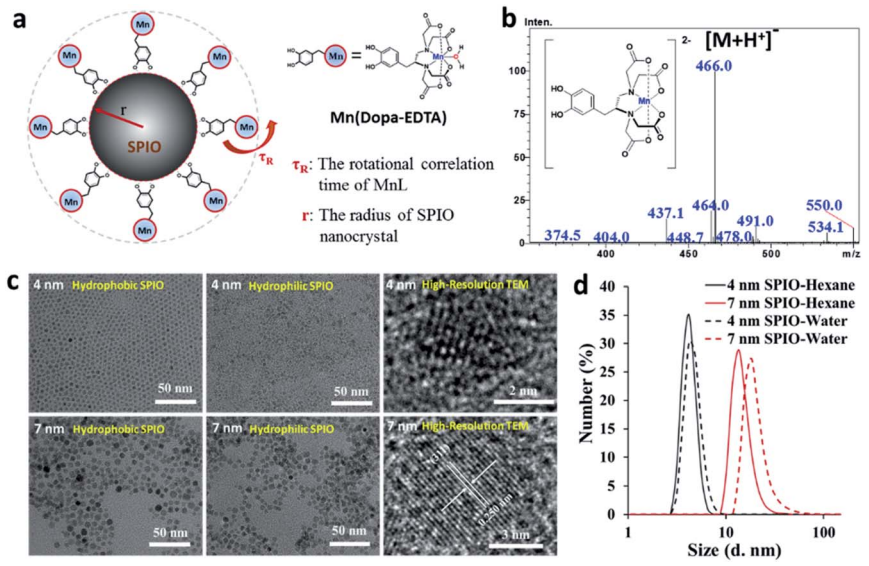

Fig. 1 Formulation of contrast agents based on $[Mn(Dopa\text{-}EDTA)]^{2-}$ and SPIO nanoparticles (SPIO@$[Mn(Dopa\text{-}EDTA)]^{2-}$). (a) Schematic illustration of SPIO@$[Mn(Dopa\text{-}EDTA)]^{2-}$ nanoparticles and $[Mn(Dopa\text{-}EDTA)]^{2-}$ coating on the surface of SPIO nanocrystals by the coordination between catechol and Fe^{3+}. (b) Mass spectrum (MS) of $[Mn(Dopa\text{-}EDTA)]^{2-}$. (c) Transmission electron microscope (TEM) and high-resolution TEM (HRTEM) images of two sizes (4 nm and 7 nm) of SPIO nanoparticles. Hydrophobic SPIO is oleic acid coated SPIO nanoparticles, while hydrophilic SPIO is its corresponding product by ligand exchange with $[Mn(Dopa\text{-}EDTA)]^{2-}$. (d) Dynamic light scattering (DLS) diameter of the two sizes of SPIO nanoparticles before (in Hexane) and after (in Water) ligand exchange with $[Mn(Dopa\text{-}EDTA)]^{2-}$.

Table 1 The relaxivities of SPIO@[Mn(Dopa-EDTA)]$^{2-}$ nanoparticles at different magnetic fields (Room temperature)

Sample name	Relaxivities			
	B_0 [T]	r_1 [mM^{-1} s^{-1}][a]	r_2 [mM^{-1} s^{-1}][a]	r_2/r_1
4 nm SPIO@[Mn(Dopa-EDTA)]$^{2-}$	0.5	8.4	14.7	1.75
	1.5	7.1	24.2	3.41
	3.0	5.4	28.4	5.26
7 nm SPIO@[Mn(Dopa-EDTA)]$^{2-}$	0.5	25.6	99.6	3.89
	1.5	16.2	145.7	8.99
	3.0	10.0	150.0	15.00

[a] The mM represents concentrations of the total iron and manganese ions.

were named 4 nm SPIO and 7 nm SPIO. The distance between the two adjacent planes is measured to be 2.50 Å, corresponding to the (311) planes in the spinel-structured Fe_3O_4. Certainly, further the selected area electron diffraction (SAED) pattern was used to characterize the crystal structure of SPIO nanoparticles (Fig. S3†). The measured lattice spacing based on the rings in the diffraction pattern conformed to the known lattice spacing for bulk Fe_3O_4 along with their respective *hkl* indices from the PDF database (Fig. S3†). In DLS analysis (Fig. 1d), it can be observed that there is a slight increase in the number average size, from 4.2 ± 0.7 nm to 4.6 ± 0.9 nm for 4 nm SPIO and from 14.7 ± 3.8 nm to 20.5 ± 6.9 nm for 7 nm SPIO. These results depicted that SPIO nanocrystals maintained monodispersion after transfer to the water phase as a whole but a small amount of aggregation may exist which is unavoidable and often hard to find under a TEM. Zeta potential measurements in ultrapure water show −8.4 ± 2.6 mV and −27.0 ± 1.5 mV for 4 nm and 7 nm nanoparticles respectively, which ensured the stable dispersion of SPIO@[Mn(Dopa-EDTA)]$^{2-}$ nanoparticles in water. The good water solubility, monodispersion in TEM and negative zeta potentials of SPIO nanocrystals explain the successfull ligand exchange of hydrophilic [Mn(Dopa-EDTA)]$^{2-}$ with hydrophobic oleic acid on the surface of SPIO nanoparticles. Iron and manganese ion concentrations of SPIO@[Mn(Dopa-EDTA)]$^{2-}$ nanoparticle solutions were measured by inductively coupled plasma-mass spectrometry (ICP-MS), and Fe-to-Mn ratios (Fe/Mn) and the number of iron and manganese atoms per SPIO nanoparticle were calculated respectively (Table S1†). The Fe/Mn ratio depends on the specific surface area of nanoparticles, as [Mn(Dopa-EDTA)]$^{2-}$ is coated on the surface of SPIO nanocrystals. Deservedly, small size SPIO nanocrystals should have a larger specific surface, which would result in a lower Fe/Mn ratio. Fe/Mn ratios of 4 nm and 7 nm SPIO@[Mn(Dopa-EDTA)]$^{2-}$ are 5.3 and 17.4 respectively and in good accordance with theory.

In order to understand the MR contrast effect (r_2/r_1 ratio) of SPIO@[Mn(Dopa-EDTA)]$^{2-}$ nanoparticles, we measured their T_1 and T_2 relaxivities at three main common magnetic fields (0.5, 1.5 and 3.0 T) (Fig. S4 and S5†). The relaxivities were calculated with total paramagnetic metal ion concentration (total iron and manganese ions) of SPIO@[Mn(Dopa-EDTA)]$^{2-}$ nanoparticles in units of (Fe + Mn) mM^{-1} s^{-1} (Table 1). In both nanoparticle groups, r_1 decreased with the increase of magnetic field (from 0.5 to 3.0 T). On the contrary, r_2 gradually increased in the same field range, and resulted in the increase of r_2/r_1 ratio. This phenomenon indicated that T_2 relaxation is more effective at higher fields which reflected the ability of the CA to produce local magnetic inhomogeneities. Overall, both the SPIO@[Mn(Dopa-EDTA)]$^{2-}$ nanoparticles have superior r_1 and r_2 values, and are typical T_1–T_2 dual-modal CAs in the appropriate magnetic field (3.0 T for 4 nm SPIO@[Mn(Dopa-EDTA)]$^{2-}$ and 1.5 T for 7 nm SPIO@[Mn(Dopa-EDTA)]$^{2-}$). In addition, 4 nm SPIO@[Mn(Dopa-EDTA)]$^{2-}$ with smaller r_2/r_1 = 1.75 at 0.5 T tends to be a perfect T_1 contrast agent and 7 nm SPIO@[Mn(Dopa-EDTA)]$^{2-}$ with higher r_2/r_1 = 15.0 at 3.0 T tends to be a T_2 contrast agent. The relaxivities (r_1 and r_2) of [Mn(Dopa-EDTA)]$^{2-}$ were also measured as a control at corresponding fields, and are listed in Table S2.† The results show that [Mn(Dopa-EDTA)]$^{2-}$ is only a common small molecule T_1 contrast agent in the three magnetic fields.

MRI CAs only work well with suitable imaging sequences and parameters. Herein, four types of imaging modes based on the spin-echo sequence (T_1WI, T_2WI, T_1-MAP, and T_2-MAP) carried out using a 1.5 T clinical MRI scanner to study the image quality of SPIO@[Mn(Dopa-EDTA)]$^{2-}$ nanoparticles *in vitro*. Fig. 2a and c show T_1WI and T_1-MAP of SPIO@[Mn(Dopa-EDTA)]$^{2-}$ aqueous solutions with different concentrations. T_1WI imaging (TR = 200 ms, TE = 9 ms) depicted that signal intensity (SI)

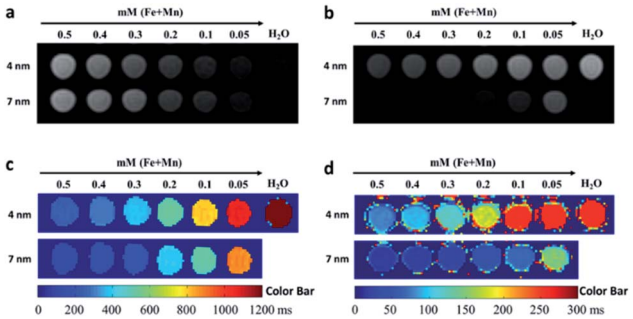

Fig. 2 MR images of SPIO@[Mn(Dopa-EDTA)]$^{2-}$ nanoparticles *in vitro*. (a) T_1WI (spin-echo sequence: TR = 200 ms, TE = 9 ms, slice thickness = 3 mm, flip angle = 90°), (b) T_2WI (spin-echo sequence: TR = 2500 ms, TE = 100 ms, slice thickness = 3 mm, flip angle = 90°), (c) T_1-MAP and (d) T_2-MAP of the two sizes of SPIO@[Mn(Dopa-EDTA)]$^{2-}$ nanoparticles in aqueous solution with different concentrations with a 1.5 T commercial MRI scanner.

increased with the concentration of SPIO@[Mn(Dopa-EDTA)]$^{2-}$ nanoparticles, but there was no visual difference in the variation trend between 4 nm and 7 nm SPIO@[Mn(Dopa-EDTA)]$^{2-}$ nanoparticles, though the r_1 of 7 nm SPIO@[Mn(Dopa-EDTA)]$^{2-}$ is apparently higher than that of 4 nm SPIO@[Mn(Dopa-EDTA)]$^{2-}$ (Table 1). This is because 7 nm SPIO@[Mn(Dopa-EDTA)]$^{2-}$ solutions show shorter T_1 and T_2 simultaneously than 4 nm SPIO@[Mn(Dopa-EDTA)]$^{2-}$ solutions at the same concentration, which produce similar SI in this T_1WI imaging. To achieve distinct T_1WI imaging, much lower TE values must be set, like ultra-short TE.[56,57] However, the variation trend of enhanced relaxation can be recognized in T_1-MAP more obviously (Fig. 2c). Fig. 2b and d show T_2WI and T_2-MAP of SPIO@[Mn(Dopa-EDTA)]$^{2-}$ aqueous solution, and SI is obviously varied. These results show that the 7 nm system is more effective than the 4 nm one in both T_1-MAP and T_2-MAP imaging modes, but the contrast enhancement in T_1WI or T_2WI imaging depends also on imaging parameters (TE and TR), especially for T_1WI imaging.

The biodistribution, clearance and imaging effect of MRI CAs were heavily determined from their stability and the interactions with proteins in plasma once entering the bloodstream. SPIO@[Mn(Dopa-EDTA)]$^{2-}$ nanoparticles show good stability in plasma with their surface coated with negative charge [Mn(Dopa-EDTA)]$^{2-}$. To further evaluate their serum stability, we monitored the size changes of SPIO@[Mn(Dopa-EDTA)]$^{2-}$ in DLS after being incubated with 20% (v/v) fetal bovine serum (FBS) solution at 37 °C for 5 h. The size increase with incubation time is observed in the presence of FBS (Fig. S6†), though visible precipitation did not occur in the whole experiment. The results state that nonspecific adsorption still exists on the surface of SPIO@[Mn(Dopa-EDTA)]$^{2-}$ after long time incubation in serum proteins. The cytotoxicity of SPIO@[Mn(Dopa-EDTA)]$^{2-}$ nanoparticles was evaluated by CCK-8 assay on mouse macrophage cell line Raw 264.7. Fig. S7† shows the cytotoxicity of 4 nm and 7 nm SPIO@[Mn(Dopa-EDTA)]$^{2-}$ after incubation for 24 h. The results indicate that low concentration SPIO@[Mn(Dopa-EDTA)]$^{2-}$ (below 10 μg mL^{-1}) promoted growth of Raw 264.7 cells, and cell growth was restrained with increasing SPIO@[Mn(Dopa-EDTA)]$^{2-}$ nanoparticle concentration. This phenomenon states that Fe and Mn are necessary trace elements in the living body and benefit cell reproduction at suitable concentrations. 4 nm SPIO@[Mn(Dopa-EDTA)]$^{2-}$ shows more toxic effects than 7 nm SPIO@[Mn(Dopa-EDTA)]$^{2-}$ at high concentrations, maybe the result of its high [Mn(Dopa-EDTA)]$^{2-}$ content.

Contrast enhanced MRA (CEMRA) is an important T_1 weighted imaging method to detect cardiovascular system diseases in clinics, such as arterial aneurysm, vascular malformation and tumor angiogenesis. Based on the excellent T_1 relaxivity of SPIO@[Mn(Dopa-EDTA)]$^{2-}$ nanoparticles, CEMRA was performed on SD rats to evaluate their vascular structure, contrast enhancement, and tissue distribution *in vivo*. Fig. 3a shows the MR images of SD rats before and after intravenous injection of 4 nm SPIO@[Mn(Dopa-EDTA)]$^{2-}$ nanoparticles with the CEMRA sequence. The cardiac and vascular lumen can be enhanced over a long period time with these nanoparticles (lasting about 2.5 h) (Fig. S8†). The signal intensities (SI) in the

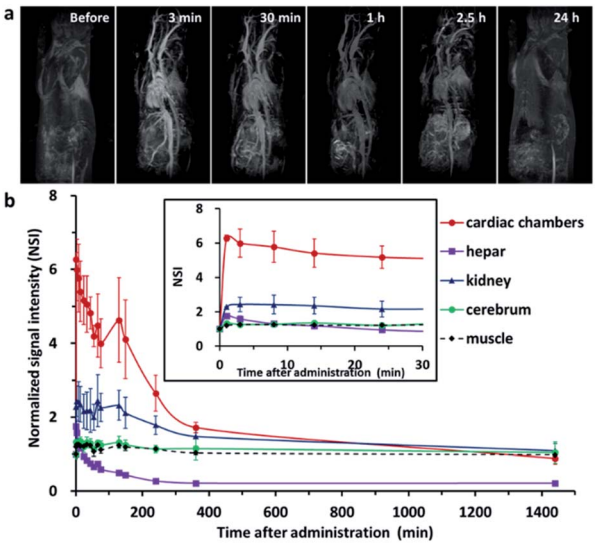

Fig. 3 MRI dynamic contrast-enhanced effect of SPIO@[Mn(Dopa-EDTA)]$^{2-}$ nanoparticles *in vivo*. (a) MRA images (TR = 6 ms, TE = 2 ms, field of view = 140 mm × 140 mm, slices = 72, slice thickness = 0.8 mm, Flip Angle = 30°) of SD rats; (b) normalized signal intensities (NSI) in the cardiac chamber, liver parenchyma, renal parenchyma, cerebrum and muscle in MRA images at different time points.

cardiac chamber, liver parenchyma, renal parenchyma, cerebrum and muscles at different time points were measured and were normalized to SI prior to contrast agent injection. The change of normalized signal intensity (NSI) with time is depicted in Fig. 3b. From the NSI-time curves, it can be observed that the signal intensities in the cardiac chamber, liver parenchyma and renal parenchyma reached the peak quickly within minutes and then present different variation tendency with time. For the cardiac chamber and renal parenchyma, the signal intensities maintain a consistently high value up to 2 hours, and then decrease slowly, and finally return to the level before administration at 24 hours. However, the signal intensity in the liver parenchyma shows obviously different changes. After reaching the peak in one minute, the signal intensity constantly decreases with time, and maintains a very low signal for more than 24 hours. In addition, the cerebrum and muscles maintain a constant slightly enhancement for several hours after administration. These results show that SPIO@[Mn(Dopa-EDTA)]$^{2-}$ nanoparticles are an excellent MRA agent with a very long imaging time window, owing to their high longitudinal relaxivity (r_1) and nano-size effect, which cannot be achieved by a small molecular contrast agent, like GdDTPA (Fig. S9†). The signal intensity change in the liver parenchyma is another interesting feature. The initial signal intensity increase is the result of the SPIO@[Mn(Dopa-EDTA)]$^{2-}$ nanoparticle distribution in the hepatic microvessel. The following intensity decrease gradually may be the result of SPIO@[Mn(Dopa-EDTA)]$^{2-}$ nanoparticle accumulation in the hepatic parenchyma, which may cause aggregation of SPIO@[Mn(Dopa-EDTA)]$^{2-}$ nanoparticles and lead to a strong T_2 relaxation effect. These imaging features indicate that SPIO@[Mn(Dopa-EDTA)]$^{2-}$ nanoparticles are stable and single-dispersed in the circulating blood (induce

a bright T_1 contrast) and are gradually captured and confined by phagocytes in the liver tissue (induce a dark T_2 contrast). This conclusion was further confirmed by pathological histology of the liver (Fig. S10†). Prussian blue staining showed plenty of blue iron particles located in the hepatic tissue, which were extracted from rats at 24 hours after administration of SPIO@[Mn(Dopa-EDTA)]$^{2-}$ nanoparticles. Similar results can also be found in previous reports.[18,21]

At 3.0 T, 4 nm SPIO@[Mn(Dopa-EDTA)]$^{2-}$ nanoparticles with an intermediate r_2/r_1 ratio (5.26) serve as T_1–T_2 dual-modal CAs. For further verification of the T_1–T_2 dual-modal enhancement of SPIO@[Mn(Dopa-EDTA)]$^{2-}$ nanoparticles *in vivo*, T_1WI and T_2WI sequences were used to study the hepatic imaging of BALB/c mice simultaneously. Fig. 4a shows the imaging results before and after administration of 4 nm SPIO@[Mn(Dopa-EDTA)]$^{2-}$ nanoparticles. The liver tissue area reveals hyperintensity in T_1WI and hypointensity in T_2WI after administration, and the hepatic vessels and gallbladder are visible in the T_1–T_2 dual-modal imaging. Fig. 4b and c show that the signal changes are obvious in the liver tissues before and after administration, and the SNR increase is 64.6 ± 18.7% for T_1WI and the decrease is 41.7 ± 4.2% for T_2WI respectively. These results indicate that SPIO@[Mn(Dopa-EDTA)]$^{2-}$ has potential to serve as a T_1–T_2 dual-modal MRI CA for liver imaging, which may be helpful for accurate diagnosis of liver lesions, like tumors and nodules.

All animal procedures were performed in accordance with the Guidelines for Care and Use of Laboratory Animals of North Sichuan Medical College and experiments were approved by the Animal Ethics Committee of North Sichuan Medical College.

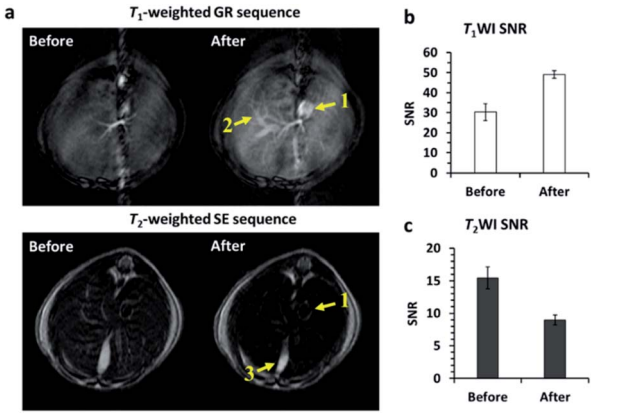

Fig. 4 Mouse hepatic T_1–T_2 dual-modal imaging before and after intravenous injection of 4 nm SPIO@[Mn(Dopa-EDTA)]$^{2-}$. (a) T_1WI (GR sequence: TR = 9.9 ms, TE = 3.5 ms, field of view = 60 mm × 60 mm, matrix = 512 × 512, slice thickness = 1.8 mm, flip angle = 30°) and T_2WI (SE sequence: TR = 4000 ms, TE = 101 ms, field of view = 60 mm × 60 mm, matrix = 512 × 512, slice thickness = 1 mm, flip angle = 142°) before and after administration of 4 nm SPIO@[Mn(Dopa-EDTA)]$^{2-}$ with a dose of 0.03 mmol (Fe + Mn)/Kg body weight with a clinical 3.0 T MRI scanner. The inferior vena cava (1), portal vein (2), and gallbladder (3) were enhanced significantly; (b) SNR in the hepatic tissue for T_1WI; (c) SNR in the hepatic tissue for T_2 WI (n = 3. Data represent mean ± s day). The results show that the signal changes (ΔSNR) in the hepatic tissue are 64.6 ± 18.7% and 41.7 ± 4.2% for T_1WI and T_2WI respectively.

Conclusions

We have developed a new non-gadolinium-based nano-scale MRI contrast agent SPIO@[Mn(Dopa-EDTA)]$^{2-}$ nanoparticles based on the catechol chemistry strategy. Our study has shown that 4 and 7 nm SPIO@[Mn(Dopa-EDTA)]$^{2-}$ nanoparticles show excellent MRI relaxation performance and different relaxation behavior at 0.5, 1.5 and 3.0 T to be fit for use as T_1, T_2 or T_1–T_2 dual-modal contrast agents. 4 nm SPIO@[Mn(Dopa-EDTA)]$^{2-}$ nanoparticles with an appropriate value of r_2/r_1 (5.26) at 3.0 T can serve as T_1–T_2 dual-modal MRI contrast agents to produce the synergistic tissue contrast enhancement and long-acting vascular imaging *in vivo*. These nanoparticles may provide a useful method for human organ and vascular MR imaging with their ease of synthesis, good biocompatibility, and unique imaging features *in vivo*.

Conflicts of interest

There are no conflicts to declare.

Acknowledgements

The work was supported by the National Natural Science Foundation of China (81601490 and 81671675), Science and Technology Project of Sichuan, China (2016JY0172), Science and Technology Project of Municipal School Strategic Cooperation, Nanchong (NSMC20170101, NSMC20170430 and 18SXHZ0091), Scientific Research Start-up Fund of North Sichuan Medical College (CBY15-QD02), and Pre-research Project of North Sichuan Medical College (CBY19-YZ05).

Notes and references

1 M. Rudin and R. Weissleder, *Nat. Rev. Drug Discovery*, 2003, **2**, 123–131.
2 G. Yves, H. Aline, G. Pierre and V. Q. Lam, *J. Phys. D: Appl. Phys.*, 2010, **43**, 213001.
3 P. Caravan, J. J. Ellison, T. J. McMurry and R. B. Lauffer, *Chem. Rev.*, 1999, **99**, 2293–2352.
4 J. Tang, Y. Sheng, H. Hu and Y. Shen, *Prog. Polym. Sci.*, 2013, **38**, 462–502.
5 R. B. Lauffer, *Chem. Rev.*, 1987, **87**, 901–927.
6 V. M. Runge and J. T. Heverhagen, *Invest. Radiol.*, 2018, **53**, 381–389.
7 H. Su, C. Wu, J. Zhu, T. Miao, D. Wang, C. Xia, X. Zhao, Q. Gong, B. Song and H. Ai, *Dalton Trans.*, 2012, 14480–14483.
8 H. Ai, C. Flask, B. Weinberg, X.-T. Shuai, M. D. Pagel, D. Farrell, J. Duerk and J. Gao, *Adv. Mater.*, 2005, **17**, 1949–1952.
9 N. Lee, D. Yoo, D. Ling, M. H. Cho, T. Hyeon and J. Cheon, *Chem. Rev.*, 2015, **115**, 10637–10689.
10 J. W. Bulte and D. L. Kraitchman, *NMR Biomed.*, 2004, **17**, 484–499.
11 Z. Zhou, R. Bai, J. Munasinghe, Z. Shen, L. Nie and X. Chen, *ACS Nano*, 2017, **11**, 5227–5232.

12 T.-H. Shin, J.-s. Choi, S. Yun, I.-S. Kim, H.-T. Song, Y. Kim, K. I. Park and J. Cheon, *ACS Nano*, 2014, **8**, 3393–3401.
13 M. Moseley, *Stroke*, 2004, **35**, 2632–2634.
14 Z. Zhou, Z. Zhao, H. Zhang, Z. Wang, X. Chen, R. Wang, Z. Chen and J. Gao, *ACS Nano*, 2014, **8**, 7976–7985.
15 Z. Zhou, C. Wu, H. Liu, X. Zhu, Z. Zhao, L. Wang, Y. Xu, H. Ai and J. Gao, *ACS Nano*, 2015, **9**, 3012–3022.
16 H. Jung, B. Park, C. Lee, J. Cho, J. Suh, J. Park, Y. Kim, J. Kim, G. Cho and H. Cho, *Nanomedicine*, 2014, **10**, 1679–1689.
17 G. Huang, H. Li, J. Chen, Z. Zhao, L. Yang, X. Chi, Z. Chen, X. Wang and J. Gao, *Nanoscale*, 2014, **6**, 10404–10412.
18 L. Wang, J. Huang, H. Chen, H. Wu, Y. Xu, Y. Li, H. Yi, Y. A. Wang, L. Yang and H. Mao, *ACS Nano*, 2017, **11**, 4582–4592.
19 C. Bai, Z. Jia, L. Song, W. Zhang, Y. Chen, F. Zang, M. Ma, N. Gu and Y. Zhang, *Adv. Funct. Mater.*, 2018, **28**, 1802281.
20 Z. Li, P. W. Yi, Q. Sun, H. Lei, H. Li Zhao, Z. H. Zhu, S. C. Smith, M. B. Lan and G. Q. M. Lu, *Adv. Funct. Mater.*, 2012, **22**, 2387–2393.
21 J. Huang, L. Wang, X. Zhong, Y. Li, L. Yang and H. Mao, *J. Mater. Chem. B*, 2014, **2**, 5344–5351.
22 X. L. Liu, C. T. Ng, P. Chandrasekharan, H. T. Yang, L. Y. Zhao, E. Peng, Y. B. Lv, W. Xiao, J. Fang, J. B. Yi, H. Zhang, K.-H. Chuang, B. H. Bay, J. Ding and H. M. Fan, *Adv. Healthcare Mater.*, 2016, **5**, 2092–2104.
23 X. Wang, Z. Zhou, Z. Wang, Y. Xue, Y. Zeng, J. Gao, L. Zhu, X. Zhang, G. Liu and X. Chen, *Nanoscale*, 2013, **5**, 8098.
24 N. Xiao, W. Gu, H. Wang, Y. Deng, X. Shi and L. Ye, *J. Colloid Interface Sci.*, 2014, **417**, 159–165.
25 Z. Zhou, D. Huang, J. Bao, Q. Chen, G. Liu, Z. Chen, X. Chen and J. Gao, *Adv. Mater.*, 2012, **24**, 6223–6228.
26 H. Cai, X. An, S. Wen, J. Li, G. Zhang, X. Shi and M. Shen, *Part. Part. Syst. Charact.*, 2015, **32**, 934–943.
27 J.-s. Choi, J.-H. Lee, T.-H. Shin, H.-T. Song, E. Y. Kim and J. Cheon, *J. Am. Chem. Soc.*, 2010, **132**, 11015–11017.
28 M.-H. Kim, H.-Y. Son, G.-Y. Kim, K. Park, Y.-M. Huh and S. Haam, *Biomaterials*, 2016, **101**, 121–130.
29 F. Li, D. Zhi, Y. Luo, J. Zhang, X. Nan, Y. Zhang, W. Zhou, B. Qiu, L. Wen and G. Liang, *Nanoscale*, 2016, **8**, 12826–12833.
30 Y.-K. Peng, C. N. P. Lui, Y.-W. Chen, S.-W. Chou, E. Raine, P.-T. Chou, K. K. L. Yung and S. C. E. Tsang, *Chem. Mater.*, 2017, **29**, 4411–4417.
31 K. H. Bae, Y. B. Kim, Y. Lee, J. Hwang, H. Park and T. G. Park, *Bioconjugate Chem.*, 2010, **21**, 505–512.
32 H. Guo, H. Sun, H. Zhu, H. Guo and H. Sun, *New J. Chem.*, 2018, **42**, 7119–7124.
33 A. Szpak, S. Fiejdasz, W. Prendota, T. Strączek, C. Kapusta, J. Szmyd, M. Nowakowska and S. Zapotoczny, *J. Nanopart. Res.*, 2014, **16**, 2678.
34 H. Yang, Y. Zhuang, Y. Sun, A. Dai, X. Shi, D. Wu, F. Li, H. Hu and S. Yang, *Biomaterials*, 2011, **32**, 4584–4593.
35 S. Fingerhut, M. Sperling, M. Holling, T. Niederstadt, T. Allkemper, A. Radbruch, W. Heindel, W. Paulus, A. Jeibmann and U. Karst, *Acta Neuropathol.*, 2018, **136**, 127–138.
36 T. Kanda, T. Fukusato, M. Matsuda, K. Toyoda, H. Oba, J. i. Kotoku, T. Haruyama, K. Kitajima and S. Furui, *Radiology*, 2015, **276**, 228–232.
37 M. A. Perazella, *Clin. J. Am. Soc. Nephrol.*, 2007, **2**, 200–202.
38 M. A. Perazella, *Curr. Opin. Nephrol. Hypertens.*, 2009, **18**, 519–525.
39 V. M. Runge, *Invest. Radiol.*, 2017, **52**, 317–323.
40 D. Pan, S. D. Caruthers, A. Senpan, A. H. Schmieder, S. A. Wickline and G. M. Lanza, *Wiley Interdiscip. Rev.: Nanomed. Nanobiotechnol.*, 2011, **3**, 162–173.
41 B. Drahoš, I. Lukeš and É. Tóth, *Eur. J. Inorg. Chem.*, 2012, **2012**, 1975–1986.
42 D. Pan, A. H. Schmieder, S. A. Wickline and G. M. Lanza, *Tetrahedron*, 2011, **67**, 8431–8444.
43 J. Wahsner, E. M. Gale, A. Rodríguez-Rodríguez and P. Caravan, *Chem. Rev.*, 2019, **119**, 957–1057.
44 E. M. Gale, H.-Y. Wey, I. Ramsay, Y.-F. Yen, D. E. Sosnovik and P. Caravan, *Radiology*, 2018, **286**, 865–872.
45 C. Wu, L. Yang, Z. Chen, H. Zhang, D. Li, B. Lin, J. Zhu, H. Ai and X. Zhang, *RSC Adv.*, 2017, **7**, 54603–54609.
46 E. M. Gale, I. P. Atanasova, F. Blasi, I. Ay and P. Caravan, *J. Am. Chem. Soc.*, 2015, **137**, 15548–15557.
47 C. Wu, D. Li, L. Yang, B. Lin, H. Zhang, Y. Xu, Z. Cheng, C. Xia, Q. Gong, B. Song and H. Ai, *J. Mater. Chem. B*, 2015, 1470–1473.
48 E. M. Gale, S. Mukherjee, C. Liu, G. S. Loving and P. Caravan, *Inorg. Chem.*, 2014, **53**, 10748–10761.
49 A. Forgács, R. Pujales-Paradela, M. Regueiro-Figueroa, L. Valencia, D. Esteban-Gómez, M. Botta and C. Platas-Iglesias, *Dalton Trans.*, 2017, **46**, 1546–1558.
50 J. Zhu, E. M. Gale, I. Atanasova, T. A. Rietz and P. Caravan, *Chem. – Eur. J.*, 2014, **20**, 14507–14513.
51 J. A. Davies, S. G. Dutremez, C. M. Hockensmith, R. Keck, N. Richardson, S. Selman, D. A. Smith, C. W. Ulmer, L. S. Wheatley and J. Zeiss, *Acad. Radiol.*, 1996, **3**, 936–945.
52 Q. Ye, F. Zhou and W. Liu, *Chem. Soc. Rev.*, 2011, **40**, 4244–4258.
53 C. Xu, K. Xu, H. Gu, R. Zheng, H. Liu, X. Zhang, Z. Guo and B. Xu, *J. Am. Chem. Soc.*, 2004, **126**, 9938–9939.
54 R. C. Hider and X. Kong, *Nat. Prod. Rep.*, 2010, **27**, 637–657.
55 S. Sun, H. Zeng, D. B. Robinson, S. Raoux, P. M. Rice, S. X. Wang and G. Li, *J. Am. Chem. Soc.*, 2004, **126**, 273–279.
56 O. M. Girard, J. Du, L. Agemy, K. N. Sugahara, V. R. Kotamraju, E. Ruoslahti, G. M. Bydder and R. F. Mattrey, *Magn. Reson. Med.*, 2011, **65**, 1649–1660.
57 L. Wang, X. Zhong, W. Qian, J. Huang, Z. Cao, Q. Yu, M. Lipowska, R. Lin, A. Wang, L. Yang and H. Mao, *J. Magn. Reson. Imaging*, 2014, **40**, 1071–1081.